Journal of Power Sources 227 (2013) 80–85

Contents lists available at SciVerse ScienceDirect

Journal of Power Sources

journal homepage: www.elsevier.com/locate/jpowsour

Cathode properties of $Na_3M_2(PO_4)_2F_3$ [M = Ti, Fe, V] for sodium-ion batteries

Kuniko Chihara [a], Ayuko Kitajou [b], Irina D. Gocheva [a], Shigeto Okada [a,*], Jun-ichi Yamaki [a]

[a] Institute for Materials Chemistry and Engineering, Kyushu University, 6-1 Kasuga-koen, Kasuga 816-8580, Fukuoka, Japan
[b] Research and Education Center of Carbon Resources, Kyushu University, 6-1 Kasuga-koen, Kasuga 816-8580, Japan

HIGHLIGHTS

- This is the first report about the cathode properties of $Na_3M_2(PO_4)_2F_3$ against Na or $NaTi_2(PO_4)_3$ NASICON anode.
- $Na_3V_2(PO_4)_2F_3$ has 4 V voltage plateau with 120 mAh g^{-1}, which is a rare high voltage cathode against Na.
- Reversible *c* lattice expansion/contraction of $Na_3V_2(PO_4)_2F_3$ electrodes was observed by *ex-situ* XRD during cycling.

ARTICLE INFO

Article history:
Received 19 June 2012
Received in revised form
29 September 2012
Accepted 12 October 2012
Available online 31 October 2012

Keywords:
Sodium-ion battery
VASP
$Na_3M_2(PO_4)_2F_3$
Ex-situ XRD

ABSTRACT

The compounds $Na_3M_2(PO_4)_2F_3$ [M = Ti, Fe, V] were obtained by two-step solid-state synthesis, and its electrochemical properties as cathode active materials of sodium-ion batteries were investigated. The obtained $Na_3M_2(PO_4)_2F_3$ materials were found to have a tetragonal structure with a space group, $P4_2/mnm$, and were isostructural with β-$Na_3V_2(PO_4)_2F_3$ by X-ray powder diffraction (XRD) measurements. Within this series, $Na_3V_2(PO_4)_2F_3$ in particular exhibited stability on cycling and a capacity of approximately 120 mAh g^{-1} against sodium metal. Capacity retention for this compound was 98%, even after the 40th cycle of prolonged charge/discharge measurements. *Ex-situ* XRD data for $Na_3V_2(PO_4)_2F_3$ electrodes charged and discharged at selected voltages showed that the material structure expanded along the *c* axis during charging up to 4.3 V and returned to its original dimensions after cycling. This is attributed to the extraction/insertion of Na atoms layers along the (002) *a*–*b* plane in the tetragonal structure.

1. Introduction

The demand for lithium-ion batteries has increased in recent years due to their wide applicability as power storages for portable electronic devices and electric vehicles. Lithium-inserted compounds, however, are relatively costly and lithium metal resources are currently insufficient to meet the demand. As a result, alternatives to lithium are needed to satisfy the increasing demands in the near future. To this end, sodium-ion batteries have been investigated as a promising alternative to lithium-ion batteries. It is anticipated that these will bring both economic and environmental advantages, since sodium is abundant, inexpensive, and nontoxic. However, the standard electrode potential of sodium (−2.71 V vs. SHE) is lower than that of lithium (−3.05 V vs. SHE). Furthermore, its ionic volume is almost twice that of lithium and its molecular weight is triple. Hence, it has been difficult to find an insertion host that can readily accept the repeated insertion and extraction of the relatively large sodium ion into its structure. To date, reports of active materials with a significant capacity for sodium ions and thus applicability in batteries have been limited to some special material groups such as two-dimensional layered chalcogenides with van der Waals gaps (e.g. TiS_2 [1]), layered rocksalt oxides (e.g. $NaFeO_2$ [2]) and three-dimensional chalcogenides with a corner sharing matrix (e.g. FeS_2 [3]). Recently, $NaVPO_4F$ was reported as a cathode for sodium-ion batteries and showed a discharge capacity of approximately 80 mAh g^{-1} within the voltage range of 4.3–2.0 V [4]. An another sodium-based fluorophosphate, Na_2FePO_4F, has been studied as a cathode in sodium-ion batteries and exhibited a capacity of approximately 110 mAh g^{-1}, corresponding to 90% of the theoretical capacity of the one electron redox reaction between Fe^{2+} and Fe^{3+} [5]. In addition, $Na_3V_2(PO_4)_2F_3$ [6–8] has been investigated as a cathode active material of lithium-ion hybrid batteries and has shown excellent electrochemical properties. Although such sodium-inserted materials may work as cathodes against lithium metal with a lithium-containing electrolyte, these cathode active materials are sometimes not applicable in sodium-ion battery systems because of the larger sodium-ion volume.

* Corresponding author. Tel./fax: +81 92 583 7841.
E-mail address: s-okada@cm.kyushu-u.ac.jp (S. Okada).

0378-7753/$ – see front matter © 2012 Elsevier B.V. All rights reserved.
http://dx.doi.org/10.1016/j.jpowsour.2012.10.034

In this study, we focused on the series of the $Na_3M_2(PO_4)_2F_3$ [M = Ti, Fe, V] compounds and investigated their electrochemical properties for sodium-ion batteries. In addition, *ex-situ* XRD measurements of electrodes after charging and/or discharging at selected voltages, were carried out in order to examine the structural changes accompanying Na^+ extraction from the structure. For an advanced discussion, we performed structure energy calculations using the Vienna *Ab initio* Simulation Package (VASP) to elucidate the Na^+ extraction/insertion mechanism in the $Na_3V_2(PO_4)_2F_3$ structure during cycling.

2. Experimental

2.1. Study of $Na_3M_2(PO_4)_2F_3$ [M = Ti, Fe, V]

The $Na_3M_2(PO_4)_2F_3$ [M = Ti, Fe, V] compounds were prepared according to a conventional solid-state synthesis for metal phosphate compounds [9]. Either V_2O_5 (Nacalai Tesque Inc.) or Ti_2O_3 (Sigma–Aldrich) and $(NH_4)_2HPO_4$ (Wako Pure Chemical Industries) were mixed in a stoichiometric ratio, placed in a crucible, and heated at 650–950 °C for 15 h under a flow of 5% H_2 in Ar. $FePO_4 \cdot 2H_2O$ (Sigma–Aldrich) was pretreated at 100 °C under vacuum for 3 h to remove H_2O. The obtained MPO_4 [M = Ti, Fe, V] was mixed in the stoichiometric ratio with NaF (Wako Pure Chemical Industries), palletized and calcined again at 600 °C for 2 h under Ar flow.

X-ray powder diffraction (XRD) measurements were performed on a Rigaku RINT2500 powder diffractometer using Cu-Kα radiation (50 kV and 300 mA) from $2\theta = 10–80°$ with a scanning speed of 1.0°/min with 0.02° steps. The cell parameters were calculated by the Rietveld method using RIETAN-FP software (Rigaku) based on β-$Na_3V_2(PO_4)_2F_3$ (ICDD No. 089-8485). For the electrochemical studies, the 70 wt.% synthesized $Na_3M_2(PO_4)_2F_3$ [M = Ti, Fe, V] powders were first dry-ball-milled with 25 wt.% acetylene black (DENKA) under Ar. The $Na_3M_2(PO_4)_2F_3$/C composite powder thus obtained was then mixed with a 5 wt.% PTFE teflon binder (Daikin Industries) in preparation for fabricating cathode pellets. Pellets were pressed in the form of disks approximately 15 mg in mass and 10 mm in diameter, then dried under vacuum at about 110 °C overnight before assembly of the cells. Sheet-type cathodes for the purposes of conducting rate capability tests were prepared from slurries of the $Na_3M_2(PO_4)_2F_3$/C composite powder with 5 wt.% polyvinyl difluoride (PVdF) (Kureha) binder in N-methylpyrrolidone (NMP) (Wako Pure Chemical Industries). The obtained slurry was coated on Al sheets, dried under vacuum at 80 °C for 30 min and cut to a diameter of 15 mm. The electrochemical properties of the $Na_3M_2(PO_4)_2F_3$ [M = Ti, Fe, V] compounds were evaluated using a 2032 coin-type cell with a non-aqueous electrolyte (1 M $NaClO_4$/PC, Tomiyama Pure Chemicals Industries) and a polypropylene separator (model 3501; Celgard) against sodium metal (Sigma–Aldrich). To avoid any influences due to ambient from air, all cell assembly procedures were conducted in an Ar filled glovebox. The charge/discharge measurements were carried out in galvanostatic mode with a current rate of 0.2 mA cm^{-2} within the various potential windows. All tests were performed at 25 °C.

In order to investigate the structural changes during the charge/discharge measurements, both charged and discharged electrodes were carefully removed from the cell, washed, and soaked in propylene carbonate (PC, Tomiyama Pure Chemicals Industries) for one day to remove the electrolyte. They were then dried in the Ar filled glovebox under vacuum. *Ex-situ* XRD measurements were performed on materials in various charged or discharged states using Cu-Kα radiation (50 kV and 300 mA) from $2\theta = 10–80°$ with a scanning speed of 0.15°/min with 0.02° steps. All of the *ex-situ* XRD data were obtained under Ar using an air-tight specimen holder (Bruker) in order to avoid any influences of ambient air.

$Na_3V_2(PO_4)_2F_3$ exhibited the largest discharge capacity against sodium metal and its promising characteristics were confirmed in a sodium-ion cell configuration using a $NaTi_2(PO_4)_3$ anode. NASICON-type $NaTi_2(PO_4)_3$ with a *R-3c* space group was prepared for this purpose by a previously reported method [10]. Anodes for the sodium-ion cells were prepared through the same process described above for the cathodes and assembled with the $Na_3V_2(PO_4)_2F_3$ cathode in 1 M $NaClO_4$/PC electrolyte within an Ar filled glovebox.

2.2. Calculations

Based on previously reported crystallographic data [9], the crystal structure of β-$Na_3V_2(PO_4)_2F_3$ is illustrated in Fig. 1. The structure has a three-dimensional framework consisting of $[PO_4]$ tetrahedra and VO_4F_2 octahedra linked at their corners through F atoms. Na atoms are layered along the *a–b* plane in the tetragonal $P4_2/mnm$ unit cell. In order to obtain information regarding the Na^+ extraction mechanism and the geometry of the structure, density functional theory calculations were performed using VASP [11] with plane waves as a basis set and β-$Na_3V_2(PO_4)_2F_3$ (ICDD No. 089-8485) [9] as the initial standard compound. Super cells with four molecular units were used. Geometry optimization and band structure calculations were performed using the projector augmented wave (PAW) method [12] and the generalized gradient approximation (GGA) [13] expressed by the Perdew–Burke–Ernzerhof (PBE) functional [14]. In the matrix, Na atoms occupy the 8i site, which has two different coordinates: two Na atoms in the Na1 site and one Na atom in the Na2 site. To estimate the possible one Na^+-extracted states of $Na_{(3-1)}V_2(PO_4)_2F_3$, two feasible patterns were simulated. In pattern-1, half of the Na1 ions with an occupation rate of 0.5 in the 8i site were symmetrically eliminated from the super cell whereas in pattern-2, all of the Na2 ions with an occupation rate of 0.25 in the 8i site were eliminated.

3. Results and discussion

3.1. Characterization

The crystal structures of the synthesized $Na_3M_2(PO_4)_2F_3$ [M = Ti, Fe, V] compounds were characterized via XRD. The XRD profiles for these powders are shown in Fig. 2. All the compounds had XRD patterns indicating a tetragonal structure with the space group $P4_2/$

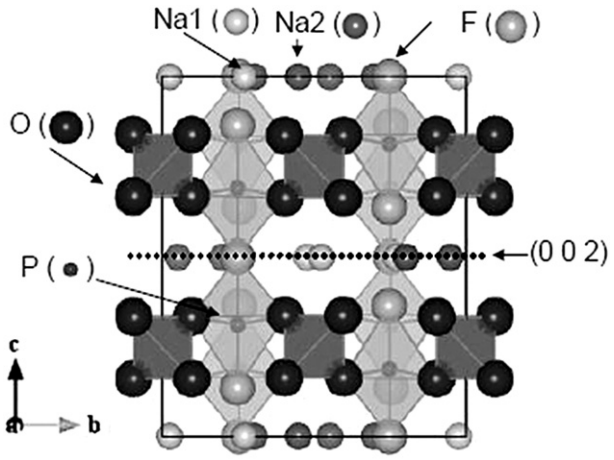

Fig. 1. Three-dimensional network of β-$Na_3V_2(PO_4)_2F_3$ viewed along the *a* axis.

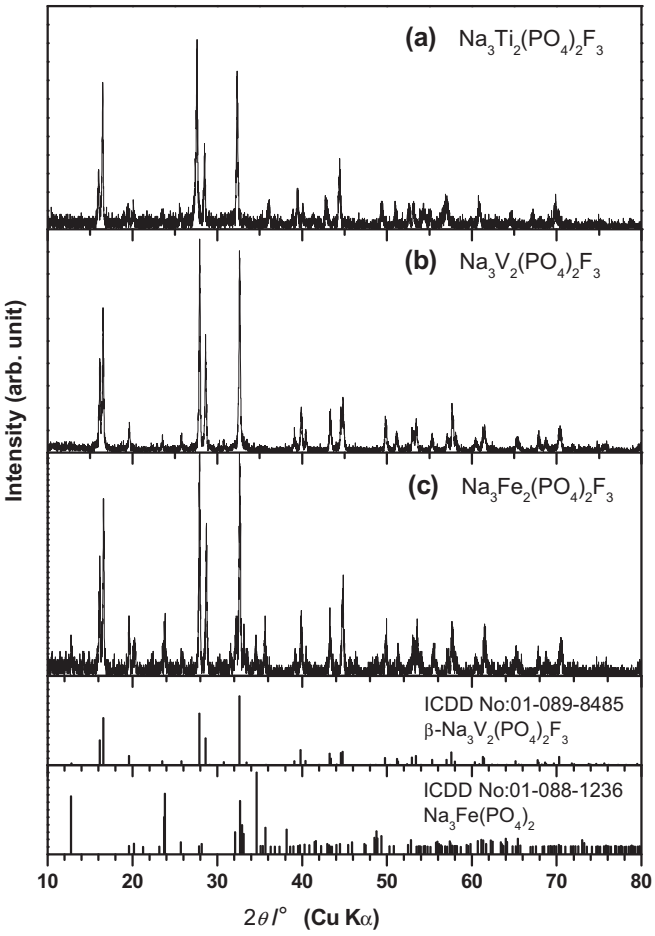

Fig. 2. XRD profiles for (a) $Na_3Ti_2(PO_4)_2F_3$, (b) $Na_3V_2(PO_4)_2F_3$, and (c) $Na_3Fe_2(PO_4)_2F_3$.

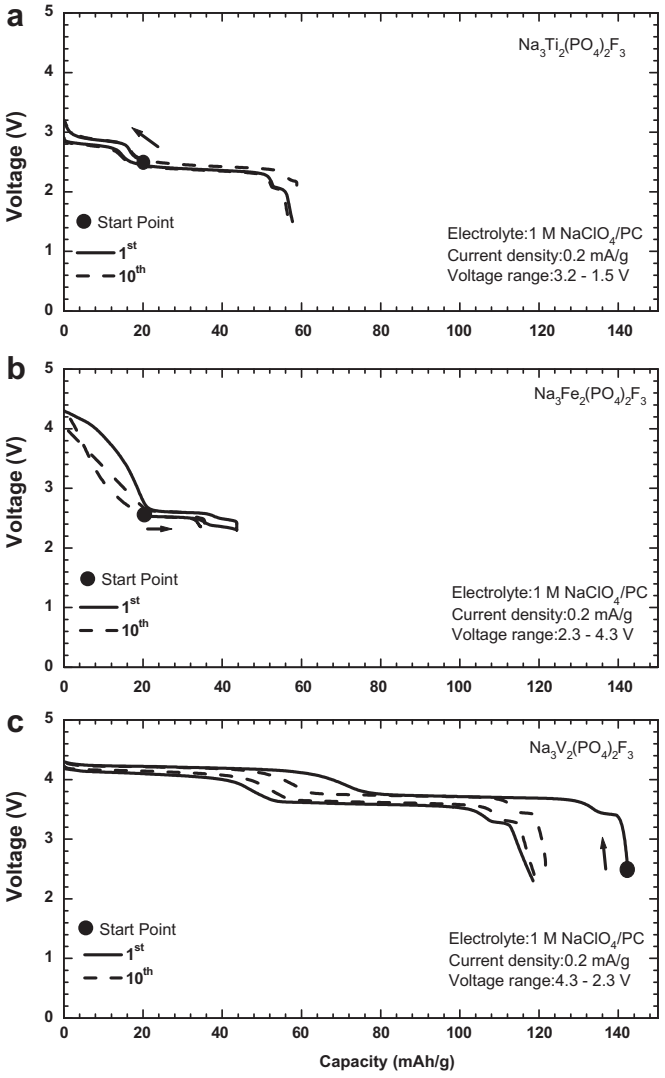

Fig. 3. First and tenth charge and discharge curves for (a) $Na_3Ti_2(PO_4)_2F_3$, (b) $Na_3Fe_2(PO_4)_2F_3$ and (c) $Na_3V_2(PO_4)_2F_3$ at a rate of 0.2 mA cm^{-2}.

mnm, and were isostructural with β-$Na_3V_2(PO_4)_2F_3$ (ICDD No. 089-8485). No major impurity phases were detected in the analysis of $Na_3Ti_2(PO_4)_2F_3$ and $Na_3V_2(PO_4)_2F_3$. $Na_3Fe_2(PO_4)_2F_3$, however, was found to contain $Na_3Fe(PO_4)_2$ (ICDD No. 01-088-1236) as an impurity.

3.2. Electrochemical properties of $Na_3M_2(PO_4)_2F_3$ [M = Ti, Fe, V]

Charge/discharge cycling of $Na_3Ti_2(PO_4)_2F_3$, $Na_3V_2(PO_4)_2F_3$ and $Na_3Fe_2(PO_4)_2F_3$ was carried out within the voltage ranges of 3.2–1.5 V, 4.3–2.3 V and 2.3–4.3 V, respectively. Fig. 3(a) shows the first and tenth charge and discharge curves for $Na_3Ti_2(PO_4)_2F_3$. During cycling, this compound exhibited a first discharge capacity of 57.7 mAh g^{-1} with two extraction/insertion plateaus at 2.7 V and 2.4 V with both of these regions demonstrating stability during cycling. This compound was also found to have a small voltage gap and irreversible capacity between charge and discharge. Fig. 3(b) shows the first and tenth charge and discharge curves for $Na_3Fe_2(PO_4)_2F_3$, which was started from discharging. The first discharge and charge capacity of $Na_3Fe_2(PO_4)_2F_3$ were 23.64 mAh g^{-1} and 43.66 mAh g^{-1}, respectively and this poor performance would be attributed to the low conductivity of this compound. Further modifications, such as the carbon-coating method reported in the case of $LiFePO_4$/C composite [15], might be necessary to improve the performance of this material. Fig. 3(c) shows the first and tenth charge and discharge curves of $Na_3V_2(PO_4)_2F_3$. Within the $Na_3M_2(PO_4)_2F_3$ [M = Ti, Fe, V] series, $Na_3V_2(PO_4)_2F_3$ showed the largest rechargeable capacity, about 120 mAh g^{-1}, in charging up to 4.3 V with two-step discharge voltage plateaus at 4.1 V and 3.6 V. Figs. 4 and 5 show the charge/discharge profiles and cycle performance of $Na_3V_2(PO_4)_2F_3$ with different cutoff voltage from 1.0 V to 4.6 V. Surprisingly, $Na_3V_2(PO_4)_2F_3$ showed good cyclability between 2.3 V and 4.6 V even after the 40th cycle, achieving 115.12 mAh g^{-1}, corresponding to 94% of the initial discharge capacity. In addition, another discharge plateau around 1.2 V is evident in the potential window down to 1.0 V, corresponding to the V^{2+}/V^{3+} redox reaction (Fig. 4(b)).

Fig. 6 shows the XRD profiles of the $Na_3V_2(PO_4)_2F_3$ electrodes both initially (Fig. 6(a)) and after 15 cycles, with cycling between 4.1 and 2.3 V (Fig. 6(b)), 4.3–2.3 V (Fig. 6(c)) and 4.6–2.3 V (Fig. 6(d)). The tetragonal structure of $Na_3V_2(PO_4)_2F_3$ was maintained even after the 15th cycle within the voltage range of 4.6–2.3 V (Fig. 6(d)). No other distinct phase was generated during the repeated cycling over this wide voltage range, suggesting that this structure is flexible enough to accommodate the structural changes accompanying the extraction/insertion of the large sodium ions.

The rate capability of $Na_3V_2(PO_4)_2F_3$ was evaluated with sheet-type electrodes prepared as described in the experimental section. The sheet-type electrodes of approximately 5 mg in total

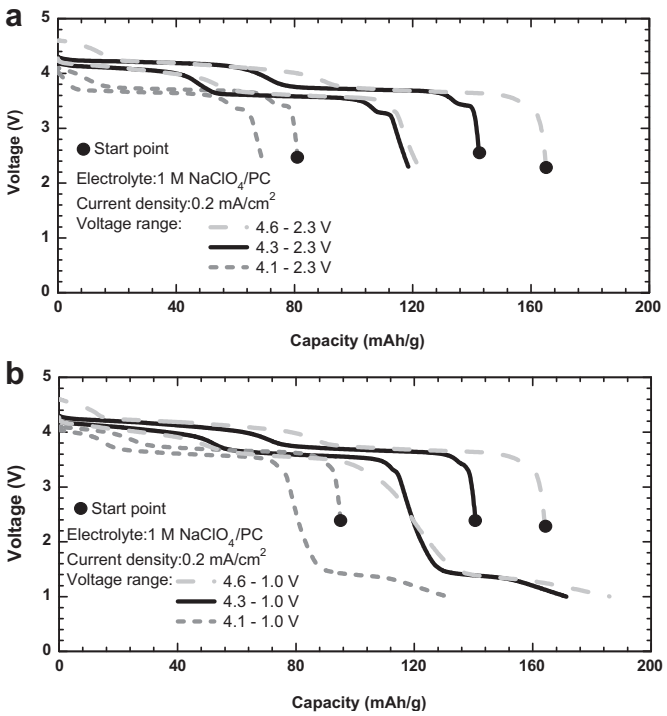

Fig. 4. First charge and discharge curves for $Na_3V_2(PO_4)_2F_3$ within the voltage ranges of (a) 4.1–2.3 V, 4.3–2.3 V and 4.6–2.3 V and (b) 4.1–1.0 V, 4.3–1.0 V and 4.6–1.0 V.

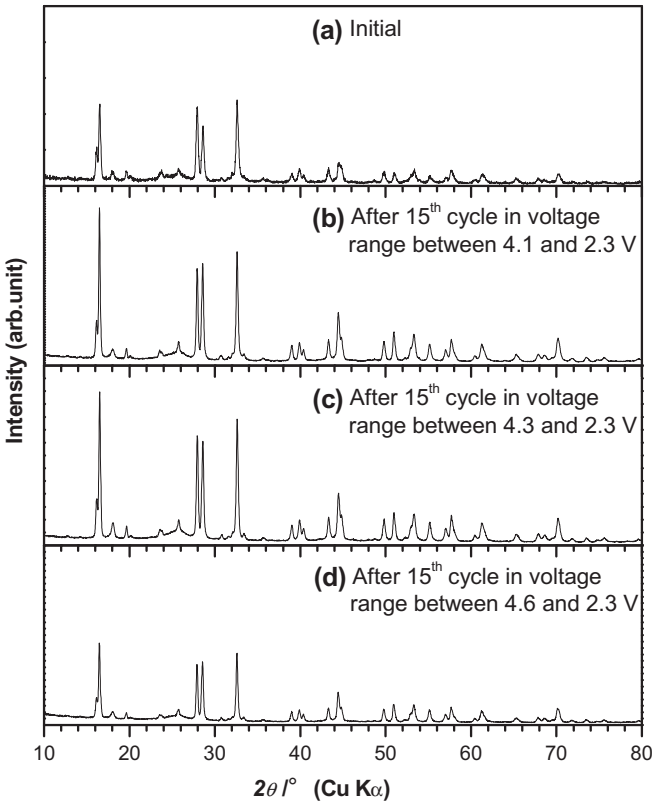

Fig. 6. XRD profiles for $Na_3V_2(PO_4)_2F_3$ in (a) initial state and after the 15th cycle within the voltage range of (b) 4.1–2.3 V, (c) 4.3–2.3 V and (d) 4.6–2.3 V.

weight (including about 3.5 mg of $Na_3V_2(PO_4)_2F_3$ as an active material) were carefully selected for the test, and a different electrode was used to study each individual rate so as to avoid any electrode damage during the charge/discharge cycling. The charge/discharge measurements were performed in galvanostatic mode. Fig. 7(a) and (b) shows the $Na_3V_2(PO_4)_2F_3$ discharging behavior dependent upon current rates against sodium metal within the voltage range of 4.3–2.3 V. In Fig. 7(a), the current density for charge and discharge was adjusted to approximate rates of 0.5 C, 1 C, 4 C, 8 C and 10 C, based on the theoretical two Na^+ extraction/insertion capacity of 128.3 mAh g^{-1}. In Fig. 7(b), however, the charging current density was fixed at 0.2 C and the varied current densities, 0.5 C, 1 C, 4 C, 8 C and 10 C, were applied to the discharge rate. $Na_3V_2(PO_4)_2F_3$ demonstrated good

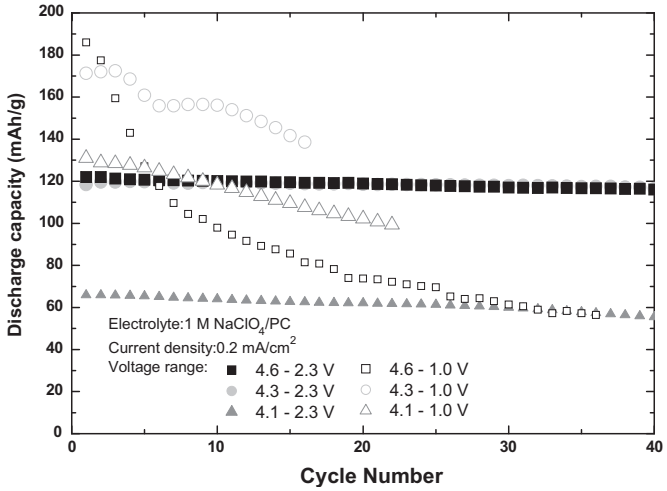

Fig. 5. Cyclability of $Na_3V_2(PO_4)_2F_3$ at different cutoff voltages from 1.0 V to 4.6 V.

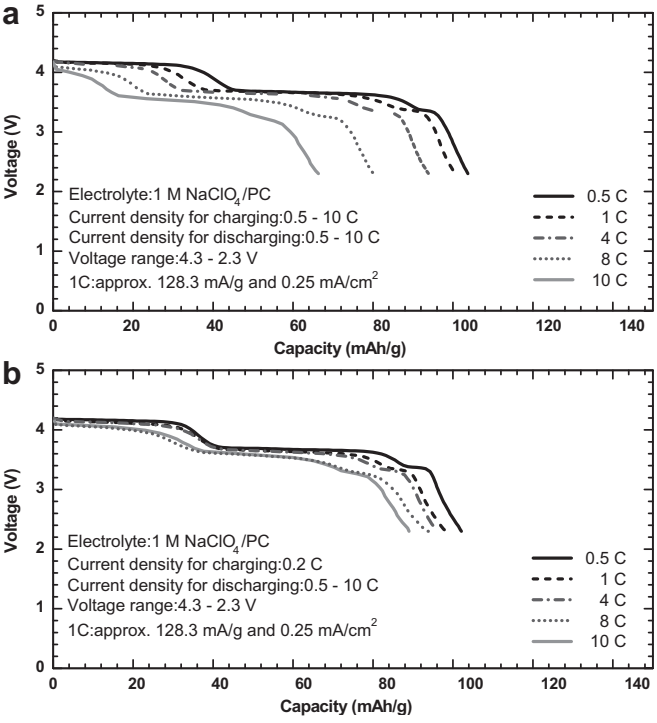

Fig. 7. Dependence of $Na_3V_2(PO_4)_2F_3$ discharge profiles upon current rates against sodium metal within the voltage range of 4.3–2.3 V.

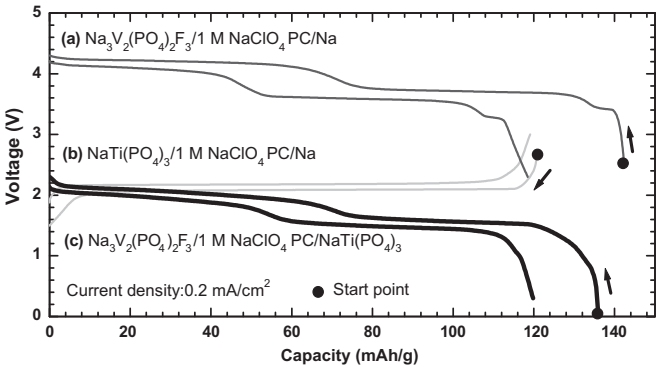

Fig. 8. First charge and discharge curves for (a) $Na_3V_2(PO_4)_2F_3$/1 M $NaClO_4$/Na, (b) $NaTi_2(PO_4)_3$/1 M $NaClO_4$/Na and (c) $Na_3V_2(PO_4)_2F_3$/1 M $NaClO_4$/$NaTi_2(PO_4)_3$ at a rate of 0.2 mA cm^{-2}. The capacity balance in the sodium-ion cell was set at a molar ratio of cathode:anode = 1:2.

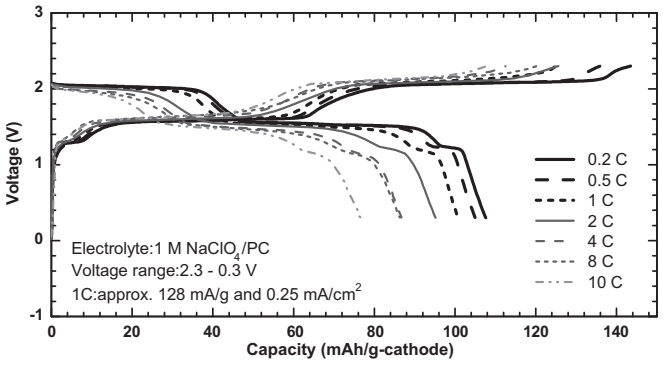

Fig. 10. Dependence of the first charge and discharge curves of the $Na_3V_2(PO_4)_2F_3$ cathode on current rates against a $NaTi_2(PO_4)_3$ anode within the voltage range of 2.3–0.3 V. Various current rates (0.5–10 C) were applied to both charging and discharging, independently.

rate capability and the initial cathode reversible capacity was more than 50% of the theoretical two Na^+ extraction/insertion capacity, even at a discharge rate of 10 C.

3.3. Electrochemical properties of $Na_3V_2(PO_4)_2F_3$ in sodium-ion batteries

$Na_3V_2(PO_4)_2F_3$ was coupled with $NaTi_2(PO_4)_3$ anodes to configure a sodium-ion cell. The $Na_3V_2(PO_4)_2F_3$/$NaTi_2(PO_4)_3$ sodium-ion cell was cycled at a current density of 0.2 mA cm^{-2} within the voltage range of 2.3–0.3 V. Fig. 8(a) and (b) shows the charge/discharge profiles of $Na_3V_2(PO_4)_2F_3$ and $NaTi_2(PO_4)_3$ in a half cell with a sodium metal anode and Fig. 8(c) shows the charge/discharge profile of the $Na_3V_2(PO_4)_2F_3$/$NaTi_2(PO_4)_3$ sodium-ion cell. The cathode-to-anode molar ratio was adjusted to 1:2, corresponding to a 1:1.9 mass ratio. In this configuration, the cell capacity is restricted by the cathode, since the theoretical capacities of $Na_3V_2(PO_4)_2F_3$ and $NaTi_2(PO_4)_3$ based on two Na^+ reaction are 128.3 mAh g^{-1} and 132.8 mAh g^{-1}, respectively. The measured first discharge capacity was 119.8 mAh g^{-1} and the stable cyclability of the cathode at approximately 110 mAh g^{-1} in this sodium-ion battery configuration was confirmed. Good capacity retention of 89.4% was exhibited, even following the 50th cycle of the prolonged charge/discharge measurements, as shown in Fig. 9. Fig. 10 shows the dependence of the cycling behavior of the $Na_3V_2(PO_4)_2F_3$ cathode upon current rates against the $NaTi_2(PO_4)_3$ anode within the voltage range of 2.3–0.3 V. The charge/discharge performance at each rate was individually studied on different cells and the rates for charge and discharge were changed from 0.2 C to 10 C simultaneously. $Na_3V_2(PO_4)_2F_3$ showed relatively good rate performance even in this sodium-ion cell configuration.

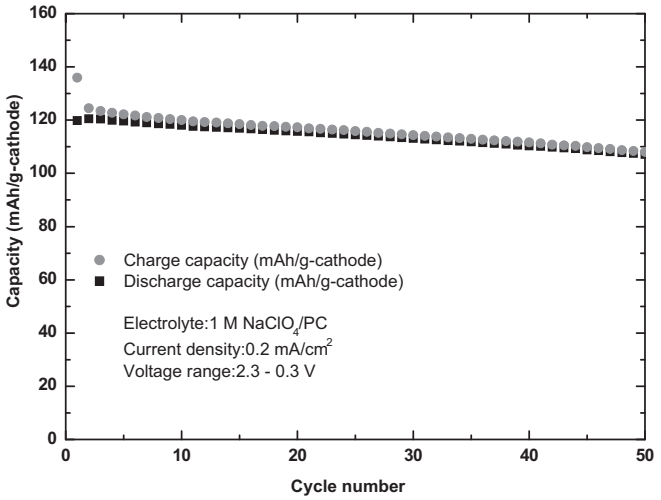

Fig. 9. Cyclability of the $Na_3V_2(PO_4)_2F_3$/1 M $NaClO_4$/$NaTi_2(PO_4)_3$ sodium-ion cell at a rate of 0.2 mA cm^{-2}.

3.4. Structural studies during cycling of $Na_3V_2(PO_4)_2F_3$

Based on the above electrochemical data for the $Na_3M_2(PO_4)_2F_3$ [M = Ti, Fe, V] series, $Na_3V_2(PO_4)_2F_3$ was determined to be a suitably representative candidate for a structural study of these compounds during charge and discharge. We therefore investigated the crystal structure changes of $Na_3V_2(PO_4)_2F_3$ accompanying the Na^+ extraction/insertion process by performing an *ex-situ* XRD measurements on the cathodes in the initial state, charged states up to 4.1 V and 4.3 V, and a cycled state to 2.3 V. Fig. 11 shows each point on the first charge/discharge cycle for the *ex-situ* XRD measurements and Fig. 12(a) shows the *ex-situ* XRD profile at the each point. All peaks were indexed to the space group $P4_2/mnm$, and obvious peak shifts were observed. The diffraction pattern of the cathode at the end of the first cycle (charge and then discharge) (Fig. 12(a-5)) returned to almost the same position as that of the initial electrode (Fig. 12(a-1)), indicating good reversibility of the cycle process. Table 1 gives the refined cell parameters of the four phases. Both *a* and *b* decreased during the charging (Fig. 12(a-2, a-3 and a-4)) and increased after the first cycle (Fig. 12(a-5)), while *c*

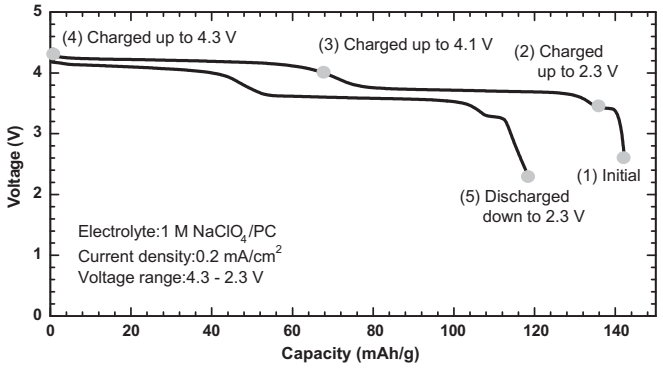

Fig. 11. *Ex-situ* XRD measuring points on the first cycle of $Na_3V_2(PO_4)_2F_3$.

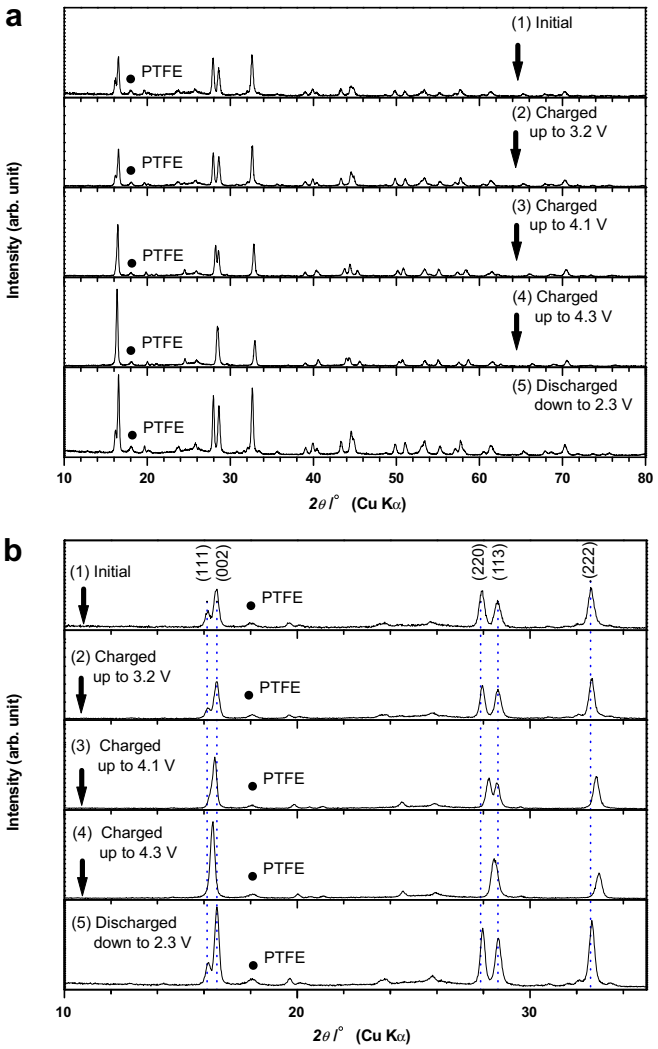

Fig. 12. (a) *Ex-situ* XRD profiles of $Na_3V_2(PO_4)_2F_3$ at (1) initial state, charged up to (2) 3.2 V, (3) 4.1 V, (4) 4.3 V, and discharged down to (5) 2.3 V after charging up to 4.3 V. (b) Expanded XRD profiles between 10 and 35°.

Table 1
Lattice parameters of $Na_{3-x}V_2(PO_4)_2F_3$ at various charge/discharge states.

Lattice parameter	ICDD	Initial state	Charged up to 4.1 V	Charged up to 4.3 V	Discharged down to 2.3 V
a	9.047	9.04	8.94	8.91	9.04
b	9.047	9.04	8.94	8.91	9.04
c	10.705	10.74	10.77	10.82	10.73
Cell volume	876.185	877.69	860.78	858.98	876.87
Δv (%)			−1.93	−2.13	−0.09

was observed to vary in a manner opposite to that of *a* and *b*, increasing during the charge and decreasing during the discharge. Enlarged *ex-situ* XRD profiles are shown in Fig. 12(b). During charging (Fig. 12(b-2, b-3 and b-4)), the (00c) peak shifted to lower angles, while the other peaks not involved with components at (00c) were shifted toward higher angles. This anisotropic lattice behavior on cycle results from the Coulomb repulsive force of Na^+ between oxygen layers along the *a*–*b* plane, since the lattice structure is changed by the inserted two-dimensional Na^+ between oxygen layers as shown in Fig. 1.

To simulate extractable sodium ions, we modeled one Na^+-extracted $Na_3V_2(PO_4)_2F_3$ structures by removing Na ions at ether the Na1 or Na2 sites from the tetragonal unit cell and then performing structural optimization via VASP. The estimated structural energies corresponding to one Na extraction from the Na1 and Na2 sites of $Na_3V_2(PO_4)_2F_3$ were −1006.00 kJ mol^{-1} and −1009.05 kJ mol^{-1}, respectively. This result suggests that Na^+ at the Na2 site is more readily extracted than that at the Na1 site, in terms of the structural energy changes.

4. Conclusion

A series of compounds corresponding to $Na_3M_2(PO_4)_2F_3$ [M = Ti, Fe, V] was prepared by a conventional solid-state synthesis and the electrochemical properties of these materials were investigated. Of these compounds, $Na_3V_2(PO_4)_2F_3$ exhibited excellent electrochemical properties. Structural analysis confirmed that this structure contracted and expanded along the *c* axis in conjunction with the extraction and insertion of sodium ions.

Acknowledgment

This work was financially supported by the Elements Science & Technology Projects of MEXT.

The authors also wish to express their appreciation for helpful advice provided by Dr. K. Chiba, Science and Technology System Division of Ryoka Systems Inc., concerning the VASP calculations presented in this work.

References

[1] M.S. Whittingham, Prog. Solid State Chem. 12 (1978) 41–99.
[2] S. Okada, S.-I. Park, Electrochemistry 79 (6) (2011) 470–476.
[3] T.B. Kim, J.W. Choi, H.S. Ryu, G.B. Cho, K.W. Kim, J.H. Ahn, K.K. Cho, H.J. Ahn, J. Power Sources 174 (2007) 1275–1278.
[4] J. Barker, M.Y. Saidi, J.L. Swoyer, Electrochem. Solid State Lett. 6 (1) (2003) A1–A4.
[5] Y. Kawabe, N. Yabuuchi, M. Kajiyama, N. Fukuhara, T. Inamasu, R. Okuyama, I. Nakai, S. Komaba, Electrochem. Commun. 13 (2011) 1225–1228.
[6] R.K.B. Gover, A. Bryan, P. Burns, J. Barker, Solid State Ionics 177 (2006) 1495–1500.
[7] J. Barker, R.K.B. Gover, P. Burns, A.J. Bryan, Electrochem. Solid State Lett. 9 (4) (2006) A190–A192.
[8] J. Barker, R.K.B. Gover, P. Burns, A.J. Bryan, J. Electrochem. Soc. 154 (9) (2007) A882–A887.
[9] J.-M. Le Meins, M.-P. Crosnier-Lopez, A. Hemon-Ribaud, G. Courbion, J. Solid State Chem. 148 (1999) 260–277.
[10] S.-I. Park, I. Gocheva, S. Okada, J. Yamaki, J. Electrochem. Soc. 158 (10) (2011) A1067–A1070.
[11] G. Kresse, J. Furthmuller, Phys. Rev. B 54 (16) (1996) 11169–11186.
[12] P.E. Blochl, Phys. Rev. B 50 (24) (1994) 17953–17979.
[13] G. Kresse, D. Joubert, Phys. Rev. B 59 (3) (1999) 1758–1775.
[14] J.P. Perdew, K. Burke, Phys. Rev. Lett. 77 (18) (1996) 3865–3868.
[15] G.T.-K. Fey, T.-L. Lu, F.-Y. Wu, W.-H. Li, J. Solid State Electrochem 12 (7–8) (2008) 825–833.